JACS
JOURNAL OF THE AMERICAN CHEMICAL SOCIETY
Article
Cite This: J. Am. Chem. Soc. 2018, 140, 7869−7877
pubs.acs.org/JACS

Photoelectrochemical CO_2 Reduction into Syngas with the Metal/Oxide Interface

Sheng Chu,[†,⊥] Pengfei Ou,[‡,⊥] Pegah Ghamari,[†,⊥] Srinivas Vanka,[†,§] Baowen Zhou,[†] Ishiang Shih,[†] Jun Song,[*,‡] and Zetian Mi[*,†,§]

[†]Department of Electrical and Computer Engineering, McGill University, 3480 University Street, Montreal, Quebec H3A 0E9, Canada

[‡]Department of Mining and Materials Engineering, McGill University, 3610 University Street, Montreal, Quebec H3A 0C5, Canada

[§]Department of Electrical Engineering and Computer Science, University of Michigan, 1301 Beal Avenue, Ann Arbor, Michigan 48109, United States

Supporting Information

ABSTRACT: Photoelectrochemical (PEC) reduction of CO_2 with H_2O not only provides an opportunity for reducing net CO_2 emissions but also produces value-added chemical feedstocks and fuels. Syngas, a mixture of CO and H_2, is a key feedstock for the production of methanol and other commodity hydrocarbons in industry. However, it is challenging to achieve efficient and stable PEC CO_2 reduction into syngas with controlled composition owing to the difficulties associated with the chemical inertness of CO_2 and complex reaction network of CO_2 conversion. Herein, by employing a metal/oxide interface to spontaneously activate CO_2 molecule and stabilize the key reaction intermediates, we report a benchmarking solar-to-syngas efficiency of 0.87% and a high turnover number of 24 800, as well as a desirable high stability of 10 h. Moreover, the CO/H_2 ratios in the composition can be tuned in a wide range between 4:1 and 1:6 with a total unity Faradaic efficiency. On the basis of experimental measurements and theoretical calculations, we present that the metal/oxide interface provides multifunctional catalytic sites with complementary chemical properties for CO_2 activation and conversion, leading to a unique pathway that is inaccessible with the individual components. The present approach opens new opportunities to rationally develop high-performance PEC systems for selective CO_2 reduction into valuable carbon-based chemicals and fuels.

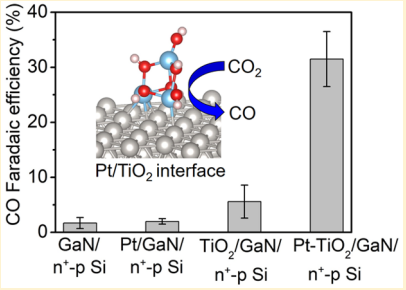

INTRODUCTION

The development of solar-powered CO_2 reduction with H_2O holds the promise to mitigate greenhouse gas (CO_2) emission into the atmosphere, while simultaneously converting renewable solar energy into storable value-added chemicals and fuels.[1−5] The photoelectrochemical (PEC) route, which combines light harvesting photovoltaic and electrochemical components into a monolithically integrated device, has received considerable attention for application in CO_2 reduction recently.[6−9] Among the wide variety of CO_2 reduction products, CO is a gaseous product that requires only two proton−electron transfers, and thus a kinetically feasible choice compared to CH_3OH and CH_4, which require six and eight proton−electron transfers to form one molecule, respectively.[10,11] Moreover, CO is an important bulk chemical to form methanol and other commodity hydrocarbons via syngas intermediate, a mixture of CO and H_2, by using well-established standard industrial processes such as Fischer−Tropsch technology.[12−15] These attributes, together with the almost inevitable H_2 evolution in aqueous PEC cell can be valorized to produce syngas mixtures, rendering the proposed syngas production from CO_2 and H_2O conversion a technologically and economically viable pathway to leverage established commercial processes for liquid fuels synthesis. Providing different CO/H_2 ratio in syngas mixtures can also be used for different downstream products (e.g., 1:3, 1:2 and 1:1 for methane, methanol and oxo-alcohols, respectively).[16−18] Therefore, the syngas route would allow a flexible platform for integration with a wide window of catalytic systems in a broad CO_2-recycling scheme without the strict requirement of suppression of H_2 evolution reaction.[19−31]

To date, various semiconductor photocathodes, including p-Si,[32−34] ZnTe,[35,36] CdTe,[37] p-InP,[37] Cu_2O[38,39] and p-NiO,[40,41] have been investigated for PEC CO_2 reduction into CO, usually in conjunction with a molecular metal-complex or metal cocatalyst (e.g., Au, Ag and derivatives) to realize selective CO production. However, it remains challenging to develop efficient and stable PEC catalytic system that can activate inert CO_2 molecule at low overpotential or even spontaneously, and selectively produce syngas with controlled composition in a wide range to meet different downstream products. It has been reported that pure metal catalyst with a simple monofunctional site usually has a weak interaction with CO_2 molecule and

Received: March 19, 2018
Published: June 15, 2018

DOI: 10.1021/jacs.8b03067
J. Am. Chem. Soc. 2018, 140, 7869−7877

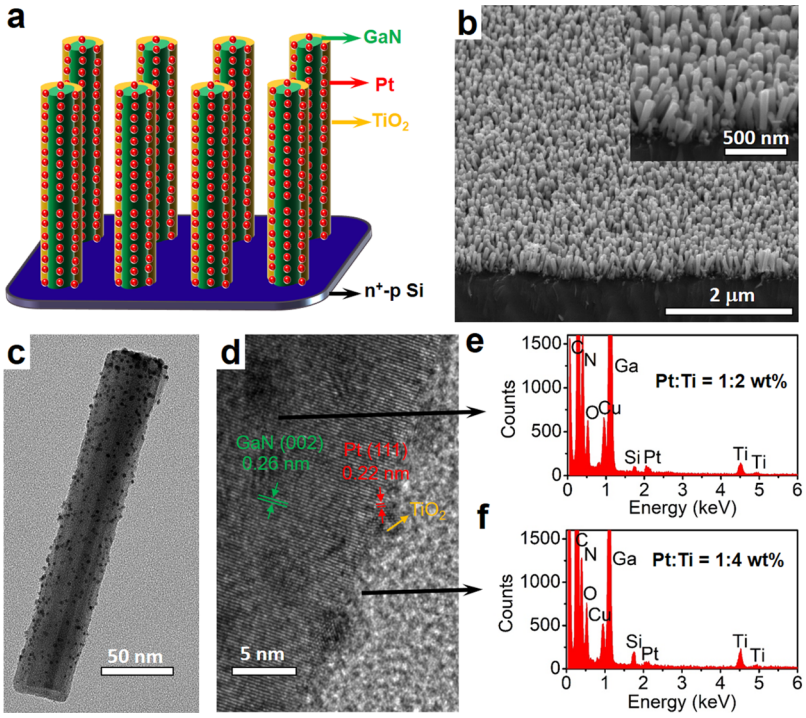

Figure 1. Characterization of Pt-TiO_2/GaN/n^+-p Si sample. (a) Schematic illustration of the structure, (b) 45°-tilted SEM image shows GaN nanowire growth vertically on the Si substrate, (c) TEM image illustrates Pt nanoparticles distributed uniformly on the GaN nanowire surface, (d) HRTEM image, and EDX analysis of the center (e) and edge region (f) indicates the coating of GaN nanowire and Pt nanoparticles with ultrathin TiO_2 layer. The Cu peaks in EDX arise from the TEM sample grid.

cannot provide multiple sites for stabilizing the key reaction intermediates with optimal binding strength, which leads to impractically high overpotential and low catalytic efficiency/stabilty.[42,43] Here we show that efficient and stable syngas production with tunable composition from PEC CO_2 reduction can be achieved with the introduction of a completely different type of sites: metal/oxide interface. On the basis of experiments and first-principles theoretical calculations, it is found that the metal/oxide interface can spontaneously activate CO_2 and stabilize the key reaction intermediates for facilitating CO production. The intimate metal/oxide interface provides the multifunctional combination of metal and oxide catalytic sites with complementary chemical properties, which opens new reaction channels that are not possible with the individual components. The versatility of using metal/oxide interface is demonstrated by the combination of different metals (Pt and Pd) and oxides (TiO_2 and ZnO). Remarkably, although pristine metal catalytically favors the proton reduction to evolve H_2, the coverage of metal with oxide to form metal/oxide interface shows preferential activity for CO_2 reduction over H_2 evolution. As an example, by rationally integrating the Pt/TiO_2 cocatalyst with the strong light harvesting of p-n Si junction and efficient electron extraction effect of GaN nanowire arrays (Pt-TiO_2/GaN/n^+-p Si), a record half-cell solar-to-syngas (STS) efficiency of 0.87% and a benchmark turnover number (TON) of 24 800 have been achieved in an aqueous PEC system. The durability of the PEC system for highly stable syngas production of 10 h has been demonstrated as well.

RESULTS AND DISCUSSION

Design and Synthesis of Pt-TiO_2/GaN/n^+-p Si. We choose Pt-TiO_2 as an example to demonstrate the validity of metal/oxide interface for PEC CO_2 reduction. GaN nanowire on p-n Si junction was selected as the platform to load the Pt-TiO_2 system. The schematic design of Pt-TiO_2/GaN/n^+-p Si is illustrated in Figure 1a. The sample was prepared in two major steps. First, GaN nanowire arrays were grown on p-n Si wafer by plasma-assisted molecular beam epitaxy (see the Supporting Information).[31,44] Such a structure takes advantage of the strong light absorption capability of Si (bandgap of 1.1 eV) and efficient electron extraction effect as well as large surface area provided by GaN nanowires. Moreover, the light absorption and catalytic reaction sites are decoupled spatially in the structure, providing an ideal platform to investigate the effect of cocatalysts on the catalytic performance without affecting the optical properties. Second, Pt nanoparticles and TiO_2 ultrathin layer were deposited on GaN nanowires surface in sequential order using photodeposition and atomic-layer deposition (ALD) process, respectively (see the Supporting Information). The intimate Pt/TiO_2 interface provides multiple sites and unique channels that facilitate the CO_2 activation and reaction pathways for syngas production.

Characterization of Structure. The morphology and chemical component of the Pt-TiO_2/GaN/n^+-p Si heterostructures were studied using scanning electron microscopy (SEM), transmission electron microscopy (TEM), energy-dispersive X-ray spectroscopy (EDX) and inductively coupled plasma−atomic emission spectroscopy (ICP-AES) analysis. The cross-sectional SEM image (Figure 1b) shows that the GaN nanowires are aligned vertically to the Si substrate with an average diameter of ∼50 nm (±15 nm) and height of 250 nm (±50 nm). TEM image in Figure 1c reveals that Pt nanoparticles of 2−3 nm size are uniformly deposited on the GaN nanowires surface. High-resolution TEM (HRTEM) image (Figure 1d), along with EDX analysis in the center and edge regions of nanowire (Figures 1e and 1f, respectively),

DOI: 10.1021/jacs.8b03067
J. Am. Chem. Soc. 2018, 140, 7869−7877

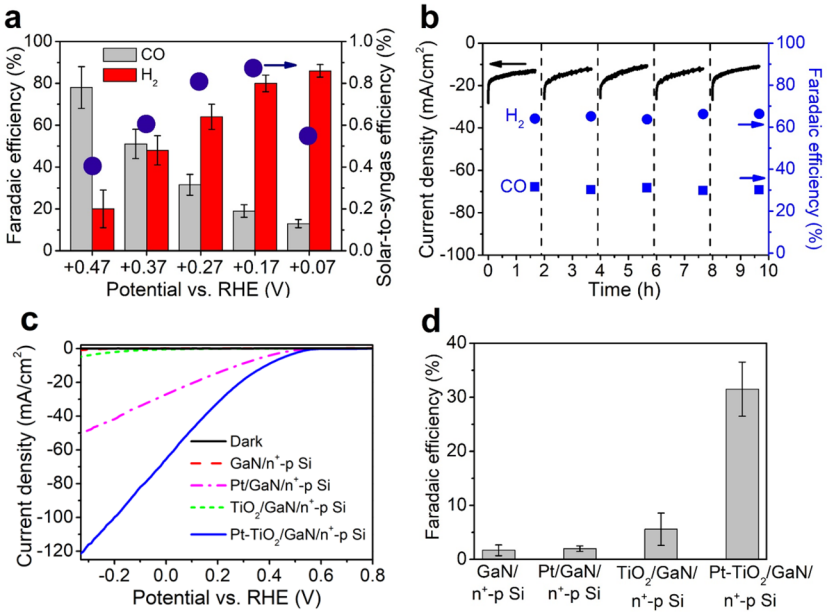

Figure 2. (a) Faradaic efficiencies for CO (gray bars) and H_2 (red bars), and solar-to-syngas efficiency of Pt-TiO_2/GaN/n^+-p Si photocathode as a function of potential in CO_2-saturated 0.5 M $KHCO_3$ solution (pH 7.5). (b) Chronoamperometry data and FEs for CO and H_2 of Pt-TiO_2/GaN/n^+-p Si photocathode at +0.27 V vs RHE. The dashed lines denote cleaning of photoelectrode and purging of the PEC cell with CO_2. (c) $J-V$ curves of bare GaN/n^+-p Si, GaN/n^+-p Si with individual Pt or TiO_2 cocatalyst, and Pt-TiO_2/GaN/n^+-p Si. (d) Faradaic efficiencies for CO at +0.27 V vs RHE. The FEs for CO of GaN/n^+-p Si and TiO_2/GaN/n^+-p Si photocathodes were measured at −0.33 V vs RHE due to the negligible photocurrent at an applied positive potential. The light illumination is ∼8 suns.

indicates the coating of GaN nanowire with ultrathin TiO_2 layer. The TiO_2 layer is amorphous and has a thickness of ∼1 nm, which corresponds to 18 ALD cycles of TiO_2 deposition. The lattice spacings of 0.22 and 0.26 nm corresponds to the (111) facet of Pt and (002) lattice plane of GaN, indicating the preferred nanowire growth along ⟨0001⟩ direction (*c*-axis). The loading amounts of Pt and Ti in Pt-TiO_2/GaN/n^+-p Si were determined to be 4.9 and 48.3 nmol cm^{-2}, respectively, by using ICP-AES analysis.

Photoelectrochemical Properties. PEC performance of the sample was investigated in CO_2-saturated 0.5 M $KHCO_3$ solution (pH 7.5) under 300 W xenon lamp irradiation (800 mW cm^{-2}, ∼8 suns) in a conventional three-electrode cell. To reveal the interaction of photocathode with CO_2, the current−potential ($J-V$) curves of Pt-TiO_2/GaN/n^+-p Si in a CO_2 or Ar-saturated electrolyte was compared (Figure S1, Supporting Information). There is a large enhancement in the photocurrent generation under CO_2 atmosphere compared to that of Ar atmosphere, indicating an interaction between the electrode surface and CO_2 molecule for CO_2 reduction. Figure 2a shows the Faradaic efficiencies (FEs) for CO and H_2 on Pt-TiO_2/GaN/n^+-p Si at applied potential between +0.47 V and +0.07 V vs reversible hydrogen electrode (RHE) in CO_2-saturated electrolyte (hereafter, all the potentials are referenced to the RHE unless otherwise specified). The corresponding chronoamperometry data at different applied potentials are shown in Figure S2 (Supporting Information). At an applied potential of +0.47 V, the photocathode exhibited a high CO FE of 78%, indicating the major extracted photogenerated electrons were used for selectively CO_2-to-CO conversion at the catalyst surface. By tuning the potential from +0.47 V to +0.07 V, the CO/H_2 ratio can be tuned in a large range between 4:1 and 1:6. At + 0.27 V, a CO/H_2 ratio of 1:2 is obtained, which is a desirable composition of syngas mixtures for methanol synthesis and Fischer−Tropsch hydrocarbon formation.[45] The decreased CO FE at a more negative potential than +0.37 V is mainly due to the limited CO_2 mass transport in the electrolyte at high CO generation rate.[46,47] The kinetic limitation was evidenced by the saturated current density for CO generation in the high applied bias region (Figure S3a, Supporting Information). In addition, different Tafel slopes for the CO_2 reduction and H_2 evolution reactions could lead to the above-mentioned bias-dependent reaction selectivity. To evaluate their contribution, the Tafel plots for CO and H_2 evolution were drawn by using the corresponding partial current density, as shown in Figure S3b in the Supporting Information. The Tafel slopes were calculated by using data points more positive than +0.37 V, as the slope increases dramatically at more negative potentials due to the mass-transport limitations.[48,49] It was found that the Tafel slopes for CO and H_2 evolution were 386 and 119 mV dec^{-1}, respectively. The different Tafel slopes result in the bias-dependent reaction selectivity largely in the low bias region. At all the applied potentials, a total FE of 97 ± 8% was obtained for the cogeneration of CO and H_2, with no appreciable amount of other gas products detected by gas chromatograph (GC) and liquid products (e.g., HCOOH and CH_3OH) analyzed by nuclear magnetic resonance (NMR) spectroscopy. To demonstrate that the generated CO from CO_2 reduction, isotopic experiment using $^{13}CO_2$ was conducted. The signal at m/z = 29 assigned to ^{13}CO appeared in the gas chromatography−mass spectrometry analysis (Figure S4, Supporting Information), indicating the CO product is formed from the reduction of CO_2.

A highlight of our system is the highly positive onset potential of +0.47 V (underpotential of 580 mV to the CO_2/CO equilibrium potential at −0.11 V) for producing high CO FE of 78% in an aqueous PEC cell. The reported onset potentials, FEs and solar energy conversion efficiency of different photocathodes for CO production in an aqueous PEC cell are compared (Table S1, Supporting Information). Among

DOI: 10.1021/jacs.8b03067
J. Am. Chem. Soc. 2018, 140, 7869−7877

various reported photocathodes, our system features the lowest onset potential, which is 170 mV positive shifted compared with the best value reported in the literature.[36] The extremely low onset potential of our photocathode is attributed to coupling effects including strong light harvesting of p-n Si junction, efficient electron extraction of GaN nanowire arrays, and extremely fast syngas production kinetics on Pt-TiO_2 dual cocatalysts. The STS efficiencies of our system at different applied potentials were calculated according to the measured photocurrent density and FEs for CO and H_2 (eq 1, Supporting Information). As shown in Figure 2a, at +0.17 V, the STS efficiency reached 0.87%, which greatly outperforms other reported photocathodes and sets a new benchmark reported to date (Table S1, Supporting Information).

The durability of Pt-TiO_2/GaN/n^+-p Si photocathode was investigated at a constant potential of +0.27 V by five consecutive runs with each run of 2 h (Figure 2b). After each cycle, the products of CO and H_2 were analyzed by GC, the electrode was thoroughly cleaned by deionized water and the PEC cell was purged by CO_2 for 20 min. During the five runs of 10 h operation, the electrode showed similar behavior in terms of photocurrent density and product selectivity, indicating the high stability of the sample during the syngas production process. The initial decrease of high photocurrent density in each run is likely due to the limited mass transfer of reactants or products at high reaction rates, which can be recovered in the next run after the cleaning of photoelectrode surface. The CO/H_2 ratio in the products was kept nearly 1:2 during the five cycles of operation, which is a desirable syngas composition for synthetizing downstream products including methanol and liquid hydrocarbons.[45] In addition, the SEM, TEM, and XPS analysis of Pt-TiO_2/GaN/n^+-p Si photocathode after the PEC reaction were performed, as shown in Figure S5 (Supporting Information). No appreciable change of GaN nanowires and Pt-TiO_2 catalysts were found. The total turnover number (TON), defined as the ratio of the total amount of syngas evolved (264 μmol) to the amount of Pt-TiO_2 catalyst (10.64 nmol, calculated from the catalyst loadings and electrode sample area of 0.2 cm^2), reached 24 800, which is at least 1 or 2 orders of magnitude higher than previously reported values for syngas or CO formation from PEC or photochemical CO_2 reduction.[31,50−53]

Investigation of the Catalytic Mechanisms. To understand the underlying catalytic mechanism and the role of basic components for the PEC performance of the Pt-TiO_2/GaN/n^+-p Si photocathode, we conducted a series of control experiments. Figure 2c shows the comparison of LSV curves for bare GaN/n^+-p Si, GaN/n^+-p Si with individual Pt or TiO_2 cocatalyst, and Pt-TiO_2/GaN/n^+-p Si. The bare GaN/n^+-p Si displays a poor PEC performance with a negligible photocurrent density and highly negative onset potential. The loading of Pt cocatalyst can greatly improve the PEC performance with an onset potential of about +0.47 V and photocurrent density of ~50 mA cm^{-2} at −0.33 V, while TiO_2 alone shows a small photocurrent density of 5 mA cm^{-2} at −0.33 V. Compared to bare Pt, significantly higher photocurrent density of ~120 mA cm^{-2} at −0.33 V is attained when Pt and TiO_2 are loaded simultaneously. It is proposed that the formation of intimate Pt/TiO_2 interface stabilizes the reaction intermediates and reduces the activation barrier for syngas production, which are validated by theoretical calculations discussed below. In addition, the ultrathin TiO_2 overlayer may passivate the nanowire surface states and reduce the probability of charge carrier recombination at the surface.[54,55] It is also supposed that Pt/TiO_2 interface is more resistant to CO poisoning than Pt alone as shown in thermochemical catalysis,[56−58] which could contribute to the enhanced syngas production on metal/oxide interface. Figure 2d shows the comparison of FEs of CO for the four samples. Besides CO product, the remaining balance of photocurrent drives H_2 evolution from proton reduction. It is shown that CO FEs are very low on bare GaN/n^+-p Si, and with individual Pt or TiO_2 cocatalyst (1.7%, 2% and 5.6%, respectively). In contrast, the CO formation selectivity increases greatly to 32% by loading Pt-TiO_2 dual cocatalyst, indicating a synergetic effect between Pt and TiO_2. We attribute the synergy to the strong interaction at the intimate metal/oxide interface, which provides the multifunctional adsorption/reaction sites for CO_2 activation and conversion. It is worth mentioning that there is an optimized thickness of ~1 nm TiO_2 for maximum catalytic activity and CO selectivity (Figure S6, Supporting Information). Very thin TiO_2 deposition yields less interfacial reactive sites, while increasing the TiO_2 thickness over 1 nm resulted in limited mass transport of reactants to the interfacial sites and large tunneling resistance to charge carrier transport associated with thick TiO_2 layer.[59,60]

CO_2 Adsorption and Activation. To elucidate the role of metal/oxide interface for the conversion of CO_2 to CO from the fundamental atomic level, density functional theory (DFT) calculations were employed using $Ti_3O_6H_6$/Pt(111) to describe the Pt/TiO_2 interface (see Supporting Information for computational details). The hydroxylation of titania cluster ($Ti_3O_6H_6$) was considered in the calculations to account for the effect of PEC CO_2 reduction conditions in an aqueous environment.[61,62] The optimized geometry of $Ti_3O_6H_6$/Pt-(111) is presented in Figure S7 (Supporting Information). As CO_2 adsorption and activation on catalyst surface is the initial and often the rate-determining step for the whole CO_2 reduction process,[63,64] we first investigate the CO_2 adsorption characteristics on $Ti_3O_6H_6$/Pt(111) surface. The calculation of CO_2 adsorption on pristine Pt(111) was also performed as a comparison. Figures 3a and 3b show the optimized configurations of CO_2 adsorption on the pristine Pt(111) and $Ti_3O_6H_6$/Pt(111) surface, respectively. It was found that CO_2 retains the original linear configuration on pristine Pt(111), similar to its isolated gas-phase state. In contrast, there are strong interactions between CO_2 molecule and the $Ti_3O_6H_6$/Pt(111) interface, with C atom strongly binding to the Pt atom underneath with a bond length of 2.02 Å and one O atom (O2) attaching to the Ti atom with a shorter bond length of 1.96 Å. Such a strong bonding between CO_2 and $Ti_3O_6H_6$/Pt(111) interface results in a significant bending of CO_2 molecule from its originally linear form to an O−C−O angle of 125.02°, thus forming a tridentate configuration that facilitates its subsequent transformations.[64] In addition, the strong interaction of CO_2 with the interface weakens the two C−O bonds of CO_2, leading to elongated C−O bonds (1.22 and 1.32 Å) from the original bond length of 1.18 Å in the isolated CO_2 molecule (Table S2, Supporting Information). The weakened C−O bonds and the formed bent CO_2 configurations indicate a remarkable activation of CO_2 molecule upon chemisorption at the interface, which is in contrast with the negligible activation of CO_2 on pristine Pt(111). This result agrees well with the observations in the field of thermochemical catalysis that CO_2 transformation is greatly enhanced with metal/oxide interface as compared to that with pure metal.[65−69] It is worth noting that the CO_2 activation mechanism at metal/oxide interface has

DOI: 10.1021/jacs.8b03067
J. Am. Chem. Soc. 2018, 140, 7869−7877

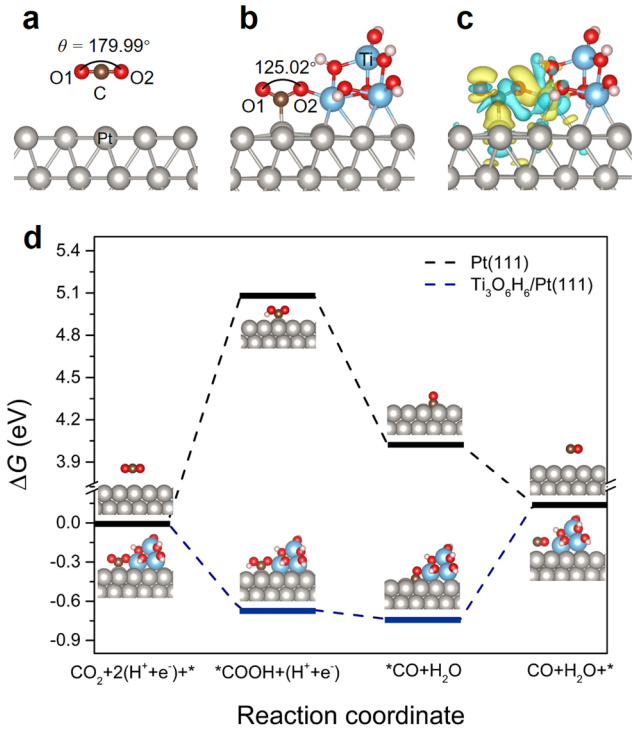

Figure 3. Side views of optimized configurations of CO_2 adsorbed on the (a) Pt(111) surface and (b) $Ti_3O_6H_6$/Pt(111) surface. (c) Differential charge density of CO_2 adsorbed at the $Ti_3O_6H_6$/Pt(111) interface. Regions of yellow and blue indicate electronic charge gain and loss, respectively. Isosurface contours of electron density differences were drawn at ±0.002 e/Bohr^3. (d) Calculated free energy diagrams for CO_2 reduction to CO on Pt(111) and $Ti_3O_6H_6$/Pt(111) surfaces at 0 V vs RHE. The optimized structures for each step are also shown. To improve legibility, a break region was added from 0.25 to 3.75 on the Y axis due to the large energy barriers for the CO_2 reduction on Pt(111) surface. Pt: gray, Ti: blue, O: red, C: brown and H: white.

a certain degree of similarity to that reported on individual metal oxide (e.g., TiO_2) with oxygen vacancies, in which one of the O atoms in CO_2 is coordinating to an undercoordinated Ti atom at the edge of the cluster (i.e., essentially an O vacancy).[70−72] For example, Somorjai and co-workers proposed a similar mechanism to explain carbonyl bond activation at the Pt/TiO_2 interface via oxygen vacancy on TiO_2 surface.[70]

The energetics associated with CO_2 adsorption on Pt(111) and $Ti_3O_6H_6$/Pt(111) surfaces were also calculated and analyzed in terms of the adsorption energy (E_{ad}) and deformation energy ($E_{def}^{CO_2}$) (Table S2, Supporting Information). Here E_{ad} represents the net energy increased upon adsorption. $E_{def}^{CO_2}$ denotes the energy change from the distortion of a linear CO_2 molecule into a buckled configuration, correlating with the degree of CO_2 activation.[73] The E_{ad} and $E_{def}^{CO_2}$ of CO_2 adsorption at $Ti_3O_6H_6$/Pt(111) interface are −0.80 and 2.65 eV respectively, as compared with those of 4.44 and 0.01 eV on pristine Pt(111). The negative E_{ad} value implies the exothermic process of CO_2 adsorption at $Ti_3O_6H_6$/Pt(111) interface, while positive E_{ad} value indicates the unfavorable CO_2 adsorption on pristine Pt(111). In addition, the large positive value of $E_{def}^{CO_2}$ in the case of $Ti_3O_6H_6$/Pt(111) confirms that CO_2 is activated spontaneously at the interface, in strong contrast to the marginal value on pristine Pt(111). Experimentally, the amount of CO_2 adsorption capacity over Pt/GaN/n^+-p Si and Pt-TiO_2/GaN/n^+-p Si was tested by CO_2 adsorption−desorption measurements (Figure S8, Supporting Information). The CO_2 adsorption amount over Pt-TiO_2/GaN/n^+-p Si was 1.91 μmol cm^{-2}, which was 7 times higher than that of Pt/GaN/n^+-p Si (0.27 μmol cm^{-2}). As a comparison, the CO_2 adsorption amount on plain GaN/n^+-p Si was 0.24 μmol cm^{-2}, indicating the low propensity of Pt for CO_2 chemisorption. The combined experimental and theoretical results explain well the different behaviors in the PEC studies that pristine Pt does not favor CO_2 reduction, while the construction of Pt/TiO_2 interface shows greatly enhanced activity for CO_2 reduction.

To further investigate the detailed bonding interaction between CO_2 and $Ti_3O_6H_6$/Pt(111) interface, the differential charge density (DCD) was examined, shown in Figure 3c. The yellow and blue regions indicate electronic charge accumulation and depletion, respectively. Strong electronic coupling between CO_2 and the interface was evidenced by the electron charge density redistribution around the interfacial region. Notable electron accumulation near the O2 atom in CO_2 and electron depletion around the neighboring Ti nucleus indicates an ionic-like Ti−O bonding, while the electron accumulation between Pt and C atoms suggests the formation of covalent Pt−C bonding. Overall, substantial electrons are transferred from the interface to CO_2 molecule, resulting in the formation of activated $*CO_2^-$ anion and eventually the enhanced CO_2 reduction activity. Quantitative estimate of the electron transfer was studied by the Bader charge analysis (Table S2, Supporting Information).[74,75] It was found that CO_2 attracted 0.684e from the substrate for CO_2 adsorption at the $Ti_3O_6H_6$/Pt(111) interface, as compared to 0.0263e in the case of pristine Pt.

Reaction Energetics. Moreover, to gain insights into the selective CO evolution from CO_2 reduction at molecular level, DFT calculations were also performed to understand the reaction energetics of the CO_2 → CO pathway. As suggested by previous studies,[76−78] we considered the following reaction steps:

$$CO_2(g) + * + H^+(aq) + e^- \rightarrow *COOH \quad (1)$$

$$*COOH + H^+(aq) + e^- \rightarrow *CO + H_2O(l) \quad (2)$$

$$*CO \rightarrow CO(g) + * \quad (3)$$

where a lone asterisk (*) represents a surface adsorption site and * symbol before a molecule denotes a surface-bound species. Figure 3d shows the calculated free energy diagram of CO_2 reduction on Pt(111) and $Ti_3O_6H_6$/Pt(111). On pristine Pt(111), the first step of CO_2 activation to form *COOH intermediate is highly endergonic with a free energy change (ΔG) of 5.08 eV, which is the rate-limiting step for the whole CO_2 reduction process. In contrast, on the $Ti_3O_6H_6$/Pt(111) interface, *COOH formation is exergonic owing to the strong binding to the interfacial sites, with C and O atoms in COOH binding to Pt(111) and Ti of $Ti_3O_6H_6$, respectively. Similarly, the strong binding and stabilization of *CO intermediates were also observed with cooperative interactions with both metal and oxide in the interface, resulting in the facile formation of *CO. The rate-limiting step in the $Ti_3O_6H_6$/Pt(111) system is the CO desorption, but with a much smaller free energy change of 0.88 eV as compared to 5.08 eV on pristine Pt(111). This result suggests that there are sites of different nature with complementary chemical properties in the metal/oxide interface that work in synergy to facilitate the CO_2 reduction into

DOI: 10.1021/jacs.8b03067
J. Am. Chem. Soc. 2018, 140, 7869−7877

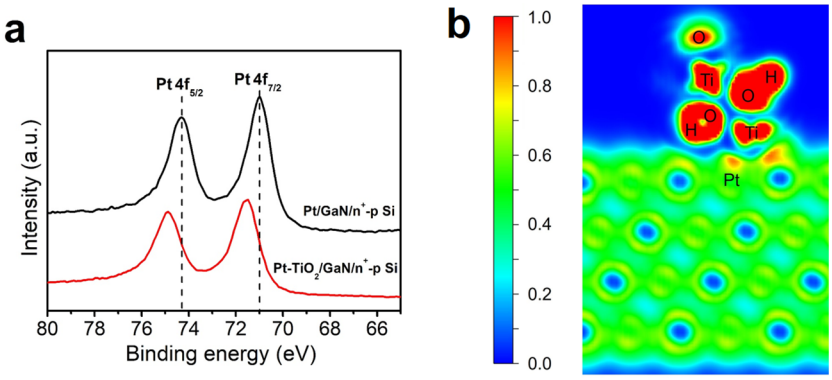

Figure 4. (a) XPS of Pt 4f of Pt/GaN/n^+-p Si and Pt-TiO_2/GaN/n^+-p Si. (b) Electron localized function (ELF) of $Ti_3O_6H_6$/Pt(111). The probability of finding electron pairs varies from 0 (blue color) to 1 (red color).

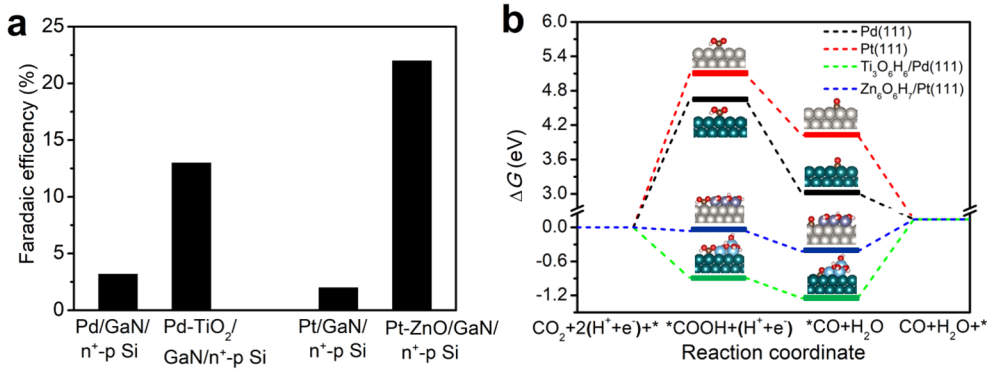

Figure 5. (a) Faradaic efficiencies for CO of Pd/GaN/n^+-p Si, Pd-TiO_2/GaN/n^+-p Si, Pt/GaN/n^+-p Si and Pt-ZnO/GaN/n^+-p Si. The measurements were performed at +0.27 V vs RHE for 100 min. (b) Calculated free energy diagrams for CO_2 reduction to CO on Pd(111), Pt(111), $Ti_3O_6H_6$/Pd(111) and $Zn_6O_6H_7$/Pt(111) surfaces at 0 V vs RHE. The optimized structures for each step are also shown. To improve legibility, a break region was added from 0.25 to 2.75 on the Y axis due to the large energy barriers for the CO_2 reduction on Pd(111) and Pt(111) surface. Pd: pine green, Pt: gray, Ti: blue, Zn: purple, O: red, C: brown and H: white.

CO. In addition, the effects of the electrolyte and applied potential were considered in DFT calculations, similar conclusions were obtained. The calculation results and details are available in the Supporting Information (Figures S9 and S10).

Considering that H_2 product from proton reduction is the other important component in the syngas mixture besides CO, we also calculated free energy diagrams for H_2 evolution on pristine Pt(111) and $Ti_3O_6H_6$/Pt(111), as shown in Figure S11a (Supporting Information). $Ti_3O_6H_6$/Pt(111) shows a slightly lowered energy barrier than that on pristine Pt(111) by 0.06 eV. Considering that the uncertainty associated with DFT energy calculations is on the same order,[79] the calculated energy barriers for hydrogen evolution reaction are comparable in the two cases. Recent studies have shown that the CO_2 reduction selectivity in competition with H_2 evolution is related to the difference between their two thermodynamic limiting potentials (denoted as $U_L(CO_2) - U_L(H_2)$).[80−82] Therefore, we have calculated the difference between limiting potentials for CO and H_2 evolution. As seen in Figure S11b (Supporting Information), $Ti_3O_6H_6$/Pt(111) displays a significantly more positive value for $U_L(CO_2) - U_L(H_2)$ than that on pristine Pt(111), indicating higher selectivity for CO_2 reduction to CO.

Strong Metal/Oxide Interaction. In addition to the important role of the metal/oxide interface in activating CO_2 and stabilizing the key reaction intermediates, the electronic modification of the Pt catalyst owing to the strong interaction between metal and oxide may also contribute to the selective CO_2 reduction into CO on Pt-TiO_2/GaN/n^+-p Si photocathode. The electronic properties of Pt were evaluated using the peak energy of Pt 4f by X-ray photoelectron spectroscopy (XPS) analysis (Figure 4a). Compared to Pt/GaN/n^+-p Si, a notable shift of ca. 0.5 eV to higher binding energy position was observed for Pt 4f in Pt-TiO_2/GaN/n^+-p Si. This shift is less pronounced than the binding energy difference between Pt^0 and Pt^{2+} in PtO (ca. 1.5 eV),[83] indicating the presence of electron deficient Pt species (Pt^{n+}) in Pt-TiO_2/GaN/n^+-p Si. A significant electronic modification by strong metal/oxide interaction is likely responsible for this change of Pt oxidation state.[84−87] To confirm the strong interaction between the metal and oxide, we computed the electron localized function (ELF) for $Ti_3O_6H_6$/Pt(111) system, as shown in Figure 4b. Topology analysis of ELF can effectively characterize the nature of different chemical bonding schemes,[88] and has been used to estimate the degree of metal−support interactions.[89] The ELF map of $Ti_3O_6H_6$/Pt(111) shows that there is a significant electron redistribution in the regions between Pt and $Ti_3O_6H_6$, indicating strong interactions between them. The strong interactions can modify the electronic property of Pt and hence enhance CO_2 reduction.

Generalization to Other Metal/Oxide Systems. By understanding the CO_2 activation and conversion at the Pt/TiO_2 interface on an atomic level, we propose that the findings can be extended to other metal/oxide systems. To show the

DOI: 10.1021/jacs.8b03067
J. Am. Chem. Soc. 2018, 140, 7869−7877

generality, Pd-TiO_2/GaN/n^+-p Si and Pt-ZnO/GaN/n^+-p Si were synthesized by varying either metal or oxide components (see the Supporting Information). The chemical components and structures were confirmed by TEM and EDX analysis (Figures S12−S13, Supporting Information). By using ICP-AES analysis, the loading amounts of Pd and Ti in Pd-TiO_2/GaN/n^+-p Si, Pt and Zn in Pt-ZnO/GaN/n^+-p Si were determined to be 5.4 and 46.1, 4.7, and 39.1 nmol cm^{-2}, respectively. The FEs of CO for Pd-TiO_2/GaN/n^+-p Si and Pt-ZnO/GaN/n^+-p Si were measured and compared with Pd/GaN/n^+-p Si and Pt/GaN/n^+-p Si, respectively (Figure 5a). The CO FEs of Pd-TiO_2/GaN/n^+-p Si and Pt-ZnO/GaN/n^+-p Si are four and 11 times higher than that with individual metal cocatalysts, similar to the trend observed in Pt-TiO_2/GaN/n^+-p Si system. In addition, the free energy diagram of CO_2 reduction into CO were calculated to validate the experimental observations. $Ti_3O_6H_6$/Pd(111) and $Zn_6O_6H_7$/Pt(111) were used in the DFT calculations to describe the Pd/TiO_2 and Pt/ZnO interface, respectively. As seen in Figure 5b, $Ti_3O_6H_6$/Pd(111) and $Zn_6O_6H_7$/Pt(111) shows a significantly lowered energy barrier than those on pristine Pd(111) and Pt(111). Similarly, it was found that the formation of *CO from CO_2 reduction via *COOH intermediate is a facile downhill process in the presence of metal/oxide interface, while the first step of CO_2 activation to form *COOH is highly endergonic on pure metal surface. Although quantitative differences exist between different systems, similar qualitative trend indicates the critical role of metal/oxide interfaces in activating CO_2, and stabilizing the key reaction intermediates for facilitating CO production. The present study could therefore provide a promising set of principles to enhance the CO_2 reduction performance by tuning the compositions and structures of metal/oxide interface.

CONCLUSIONS

In summary, we have demonstrated an efficient and stable PEC CO_2 reduction system for syngas production with controlled composition, by employing a metal/oxide interface to activate inert CO_2 molecule and stabilize the key reaction intermediates. Using Pt/TiO_2 as an example, a benchmarking solar-to-syngas efficiency of 0.87% and a high turnover number of 24 800 were achieved. Moreover, the PEC system exhibited highly stable syngas production in the 10 h duration test. On the basis of experimental measurements and theoretical calculations, it was found that the synergistic interactions at the metal/oxide interface provide unique reaction channels that structurally and electronically facilitate CO_2 conversion into CO. This work may open new opportunities for the design and development of high-performance photoelectrochemical systems for selective CO_2 reduction.

ASSOCIATED CONTENT

Supporting Information

The Supporting Information is available free of charge on the ACS Publications website at DOI: 10.1021/jacs.8b03067.

Experimental and computational methods, additional figures and tables (PDF)

AUTHOR INFORMATION

Corresponding Authors

*E-mail: jun.song2@mcgill.ca. Phone: 1 514 398 4592.
*E-mail: ztmi@umich.edu. Phone: 1 734 764 3963.

ORCID

Sheng Chu: 0000-0001-9850-5012
Jun Song: 0000-0003-3675-574X
Zetian Mi: 0000-0001-9494-7390

Author Contributions

⊥S.C., P. O., and P.G. contributed equally to this work.

Notes

The authors declare no competing financial interest.

ACKNOWLEDGMENTS

This work was supported by Emissions Reduction Alberta (ERA). Part of the work was conducted in the Microfabrication Facility at McGill University and the Michigan Center for Materials Characterization at the University of Michigan (NSF #DMR-0723032). We greatly acknowledge the financial support from McGill Engineering Doctoral Award and National Sciences and Engineering Research Council (NSERC) Discovery grant (grant # RGPIN-2017-05187). We also thank Supercomputer Consortium Laval UQAM McGill and Eastern Quebec for providing computing power.

REFERENCES

(1) Kumar, B.; Llorente, M.; Froehlich, J.; Dang, T.; Sathrum, A.; Kubiak, C. P. *Annu. Rev. Phys. Chem.* **2012**, *63*, 541.
(2) White, J. L.; Baruch, M. F.; Pander Iii, J. E.; Hu, Y.; Fortmeyer, I. C.; Park, J. E.; Zhang, T.; Liao, K.; Gu, J.; Yan, Y.; Shaw, T. W.; Abelev, E.; Bocarsly, A. B. *Chem. Rev.* **2015**, *115*, 12888.
(3) Habisreutinger, S. N.; Schmidt-Mende, L.; Stolarczyk, J. K. *Angew. Chem., Int. Ed.* **2013**, *52*, 7372.
(4) Tu, W. G.; Zhou, Y.; Zou, Z. G. *Adv. Mater.* **2014**, *26*, 4607.
(5) Xie, S. J.; Zhang, Q. H.; Liu, G. D.; Wang, Y. *Chem. Commun.* **2016**, *52*, 35.
(6) Wang, P.; Wang, S.; Wang, H.; Wu, Z.; Wang, L. *Part. Part. Syst. Char.* **2018**, *35*, 1700371.
(7) Pang, H.; Masuda, T.; Ye, J. H. *Chem. - Asian J.* **2018**, *13*, 127.
(8) Zhang, N.; Long, R.; Gao, C.; Xiong, Y. *Sci. China Mater.* **2018**, *61*, 771.
(9) Kalamaras, E.; Maroto-Valer, M.; Shao, M.; Xuan, J.; Wang, H. *Catal. Today* **2018**, DOI: 10.1016/j.cattod.2018.02.045.
(10) Vesborg, P. C. K.; Seger, B. *Chem. Mater.* **2016**, *28*, 8844.
(11) Karatairi, E.; Miller, J. E. *MRS Bull.* **2017**, *42*, 878.
(12) Bell, A. T. *Catal. Rev.: Sci. Eng.* **1981**, *23*, 203.
(13) Waugh, K. C. *Catal. Today* **1992**, *15*, 51.
(14) Dry, M. E. *Catal. Today* **2002**, *71*, 227.
(15) Khodakov, A. Y.; Chu, W.; Fongarland, P. *Chem. Rev.* **2007**, *107*, 1692.
(16) Wenzel, M.; Rihko-Struckmann, L.; Sundmacher, K. *AIChE J.* **2017**, *63*, 15.
(17) Foit, S. R.; Vinke, I. C.; de Haart, L. G. J.; Eichel, R. A. *Angew. Chem., Int. Ed.* **2017**, *56*, 5402.
(18) Hernandez, S.; Farkhondehfal, M. A.; Sastre, F.; Makkee, M.; Saracco, G.; Russo, N. *Green Chem.* **2017**, *19*, 2326.
(19) Ross, M. B.; Dinh, C. T.; Li, Y.; Kim, D.; De Luna, P.; Sargent, E. H.; Yang, P. D. *J. Am. Chem. Soc.* **2017**, *139*, 9359.
(20) Sheng, W. C.; Kattel, S.; Yao, S. Y.; Yan, B. H.; Liang, Z. X.; Hawxhurst, C. J.; Wu, Q. Y.; Chen, J. G. G. *Energy Environ. Sci.* **2017**, *10*, 1180.
(21) Xu, J. Q.; Li, X. D.; Liu, W.; Sun, Y. F.; Ju, Z. Y.; Yao, T.; Wang, C. M.; Ju, H. X.; Zhu, J. F.; Wei, S. Q.; Xie, Y. *Angew. Chem., Int. Ed.* **2017**, *56*, 9121.
(22) Guo, S. J.; Zhao, S. Q.; Wu, X. Q.; Li, H.; Zhou, Y. J.; Zhu, C.; Yang, N. J.; Jiang, X.; Gao, J.; Bai, L.; Liu, Y.; Lifshitz, Y.; Lee, S. T.; Kang, Z. H. *Nat. Commun.* **2017**, *8*, 1828.
(23) He, R.; Zhang, A.; Ding, Y. L.; Kong, T. Y.; Xiao, Q.; Li, H. L.; Liu, Y.; Zeng, J. *Adv. Mater.* **2018**, *30*, 1705872.

DOI: 10.1021/jacs.8b03067
J. Am. Chem. Soc. 2018, 140, 7869−7877

(24) Furler, P.; Scheffe, J. R.; Steinfeld, A. *Energy Environ. Sci.* **2012**, *5*, 6098.
(25) Kumar, B.; Smieja, J. M.; Sasayama, A. F.; Kubiak, C. P. *Chem. Commun.* **2012**, *48*, 272.
(26) Kang, P.; Chen, Z. F.; Nayak, A.; Zhang, S.; Meyer, T. J. *Energy Environ. Sci.* **2014**, *7*, 4007.
(27) Lee, J. S.; Won, D. I.; Jung, W. J.; Son, H. J.; Pac, C.; Kang, S. O. *Angew. Chem., Int. Ed.* **2017**, *56*, 976.
(28) Li, F. F.; Lau, J.; Licht, S. *Adv. Sci.* **2015**, *2*, 1500260.
(29) Li, D. W.; Ouyang, S. X.; Xu, H.; Lu, D.; Zhao, M.; Zhang, X. L.; Ye, J. H. *Chem. Commun.* **2016**, *52*, 5989.
(30) Urbain, F.; Tang, P. Y.; Carretero, N. M.; Andreu, T.; Gerling, L. G.; Voz, C.; Arbiol, J.; Morante, J. R. *Energy Environ. Sci.* **2017**, *10*, 2256.
(31) Chu, S.; Fan, S. Z.; Wang, Y. J.; Rossouw, D.; Wang, Y. C.; Botton, G. A.; Mi, Z. *Angew. Chem., Int. Ed.* **2016**, *55*, 14260.
(32) Hinogami, R.; Nakamura, Y.; Yae, S.; Nakato, Y. *J. Phys. Chem. B* **1998**, *102*, 974.
(33) Kong, Q.; Kim, D.; Liu, C.; Yu, Y.; Su, Y.; Li, Y.; Yang, P. D. *Nano Lett.* **2016**, *16*, 5675.
(34) Song, J. T.; Ryoo, H.; Cho, M.; Kim, J.; Kim, J. G.; Chung, S. Y.; Oh, J. *Adv. Energy Mater.* **2017**, *7*, 1601103.
(35) Jang, Y. J.; Jang, J. W.; Lee, J.; Kim, J. H.; Kumagai, H.; Lee, J.; Minegishi, T.; Kubota, J.; Domen, K.; Lee, J. S. *Energy Environ. Sci.* **2015**, *8*, 3597.
(36) Jang, Y. J.; Jeong, I.; Lee, J.; Lee, J.; Ko, M. J.; Lee, J. S. *ACS Nano* **2016**, *10*, 6980.
(37) Yoneyama, H.; Sugimura, K.; Kuwabata, S. *J. Electroanal. Chem. Interfacial Electrochem.* **1988**, *249*, 143.
(38) Torralba-Penalver, E.; Luo, Y.; Compain, J. D.; Chardon-Noblat, S.; Fabre, B. *ACS Catal.* **2015**, *5*, 6138.
(39) Schreier, M.; Luo, J. S.; Gao, P.; Moehl, T.; Mayer, M. T.; Gratzel, M. *J. Am. Chem. Soc.* **2016**, *138*, 1938.
(40) Sahara, G.; Abe, R.; Higashi, M.; Morikawa, T.; Maeda, K.; Ueda, Y.; Ishitani, O. *Chem. Commun.* **2015**, *51*, 10722.
(41) Sahara, G.; Kumagai, H.; Maeda, K.; Kaeffer, N.; Artero, V.; Higashi, M.; Abe, R.; Ishitani, O. *J. Am. Chem. Soc.* **2016**, *138*, 14152.
(42) Hansen, H. A.; Varley, J. B.; Peterson, A. A.; Norskov, J. K. *J. Phys. Chem. Lett.* **2013**, *4*, 388.
(43) Hansen, H. A.; Shi, C.; Lausche, A. C.; Peterson, A. A.; Norskov, J. K. *Phys. Chem. Chem. Phys.* **2016**, *18*, 9194.
(44) Fan, S. Z.; AlOtaibi, B.; Woo, S. Y.; Wang, Y. J.; Botton, G. A.; Mi, Z. *Nano Lett.* **2015**, *15*, 2721.
(45) Rostrup-Nielsen, J. R. *Catal. Today* **2000**, *63*, 159.
(46) Kuhl, K. P.; Hatsukade, T.; Cave, E. R.; Abram, D. N.; Kibsgaard, J.; Jaramillo, T. F. *J. Am. Chem. Soc.* **2014**, *136*, 14107.
(47) Singh, M. R.; Clark, E. L.; Bell, A. T. *Phys. Chem. Chem. Phys.* **2015**, *17*, 18924.
(48) Rosen, J.; Hutchings, G. S.; Lu, Q.; Rivera, S.; Zhou, Y.; Vlachos, D. G.; Jiao, F. *ACS Catal.* **2015**, *5*, 4293.
(49) Kim, S. K.; Zhang, Y.-J.; Bergstrom, H.; Michalsky, R.; Peterson, A. *ACS Catal.* **2016**, *6*, 2003.
(50) Takeda, H.; Ohashi, K.; Sekine, A.; Ishitani, O. *J. Am. Chem. Soc.* **2016**, *138*, 4354.
(51) Hong, D. C.; Tsukakoshi, Y.; Kotani, H.; Ishizuka, T.; Kojima, T. *J. Am. Chem. Soc.* **2017**, *139*, 6538.
(52) Rao, H.; Bonin, J.; Robert, M. *ChemSusChem* **2017**, *10*, 4447.
(53) Lian, S. C.; Kodaimati, M. S.; Weiss, E. A. *ACS Nano* **2018**, *12*, 568.
(54) Lin, Y. J.; Kapadia, R.; Yang, J. H.; Zheng, M.; Chen, K.; Hettick, M.; Yin, X. T.; Battaglia, C.; Sharp, I. D.; Ager, J. W.; Javey, A. *J. Phys. Chem. C* **2015**, *119*, 2308.
(55) Qiu, J.; Zeng, G. T.; Ha, M. A.; Ge, M. Y.; Lin, Y. J.; Hettick, M.; Hou, B. Y.; Alexandrova, A. N.; Javey, A.; Cronin, S. B. *Nano Lett.* **2015**, *15*, 6177.
(56) Hepel, M.; Kumarihamy, I.; Zhong, C. *Electrochem. Commun.* **2006**, *8*, 1439.
(57) Guo, X.; Guo, D.; Qiu, X.; Chen, L.; Zhu, W. *J. Power Sources* **2009**, *194*, 281.
(58) Shi, F.; Baker, L. R.; Hervier, A.; Somorjai, G. A.; Komvopoulos, K. *Nano Lett.* **2013**, *13*, 4469.
(59) Chen, Y. W.; Prange, J. D.; Duhnen, S.; Park, Y.; Gunji, M.; Chidsey, C. E. D.; McIntyre, P. C. *Nat. Mater.* **2011**, *10*, 539.
(60) Kim, H. J.; Kearney, K. L.; Le, L. H.; Haber, Z. J.; Rockett, A. A.; Rose, M. J. *J. Phys. Chem. C* **2016**, *120*, 25697.
(61) Kattel, S.; Yan, B. H.; Yang, Y. X.; Chen, J. G. G.; Liu, P. *J. Am. Chem. Soc.* **2016**, *138*, 12440.
(62) Gao, D.; Zhang, Y.; Zhou, Z.; Cai, F.; Zhao, X.; Huang, W.; Li, Y.; Zhu, J.; Liu, P.; Yang, F.; Wang, G.; Bao, X. *J. Am. Chem. Soc.* **2017**, *139*, 5652.
(63) Chang, X. X.; Wang, T.; Gong, J. L. *Energy Environ. Sci.* **2016**, *9*, 2177.
(64) Alvarez, A.; Borges, M.; Corral-Perez, J. J.; Olcina, J. G.; Hu, L. J.; Cornu, D.; Huang, R.; Stoian, D.; Urakawa, A. *ChemPhysChem* **2017**, *18*, 3135.
(65) Graciani, J.; Mudiyanselage, K.; Xu, F.; Baber, A. E.; Evans, J.; Senanayake, S. D.; Stacchiola, D. J.; Liu, P.; Hrbek, J.; Sanz, J. F.; Rodriguez, J. A. *Science* **2014**, *345*, 546.
(66) Rodriguez, J. A.; Liu, P.; Stacchiola, D. J.; Senanayake, S. D.; White, M. G.; Chen, J. G. G. *ACS Catal.* **2015**, *5*, 6696.
(67) Kattel, S.; Yan, B. H.; Chen, J. G. G.; Liu, P. *J. Catal.* **2016**, *343*, 115.
(68) Kattel, S.; Liu, P.; Chen, J. G. G. *J. Am. Chem. Soc.* **2017**, *139*, 9739.
(69) Kattel, S.; Ramirez, P. J.; Chen, J. G.; Rodriguez, J. A.; Liu, P. *Science* **2017**, *355*, 1296.
(70) Baker, L. R.; Kennedy, G.; Van Spronsen, M.; Hervier, A.; Cai, X.; Chen, S.; Wang, L.-W.; Somorjai, G. A. *J. Am. Chem. Soc.* **2012**, *134*, 14208.
(71) Huygh, S.; Bogaerts, A.; Neyts, E. C. *J. Phys. Chem. C* **2016**, *120*, 21659.
(72) Ji, Y. F.; Luo, Y. *J. Am. Chem. Soc.* **2016**, *138*, 15896.
(73) AlOtaibi, B.; Kong, X.; Vanka, S.; Woo, S. Y.; Pofelski, A.; Oudjedi, F.; Fan, S.; Kibria, M. G.; Botton, G. A.; Ji, W.; Guo, H.; Mi, Z. *ACS Energy Lett.* **2016**, *1*, 246.
(74) Bader, R. F. *Acc. Chem. Res.* **1985**, *18*, 9.
(75) Henkelman, G.; Arnaldsson, A.; Jónsson, H. *Comput. Mater. Sci.* **2006**, *36*, 354.
(76) Peterson, A. A.; Abild-Pedersen, F.; Studt, F.; Rossmeisl, J.; Nørskov, J. K. *Energy Environ. Sci.* **2010**, *3*, 1311.
(77) Asadi, M.; Kim, K.; Liu, C.; Addepalli, A. V.; Abbasi, P.; Yasaei, P.; Phillips, P.; Behranginia, A.; Cerrato, J. M.; Haasch, R. *Science* **2016**, *353*, 467.
(78) Li, Q.; Fu, J. J.; Zhu, W. L.; Chen, Z. Z.; Shen, B.; Wu, L. H.; Xi, Z.; Wang, T. Y.; Lu, G.; Zhu, J. J.; Sun, S. H. *J. Am. Chem. Soc.* **2017**, *139*, 4290.
(79) Wellendorff, J.; Lundgaard, K. T.; Møgelhøj, A.; Petzold, V.; Landis, D. D.; Nørskov, J. K.; Bligaard, T.; Jacobsen, K. W. *Phys. Rev. B: Condens. Matter Mater. Phys.* **2012**, *85*, 235149.
(80) Shi, C.; Hansen, H. A.; Lausche, A. C.; Nørskov, J. K. *Phys. Chem. Chem. Phys.* **2014**, *16*, 4720.
(81) Kim, D.; Xie, C. L.; Becknell, N.; Yu, Y.; Karamad, M.; Chan, K.; Crumlin, E. J.; Norskov, J. K.; Yang, P. D. *J. Am. Chem. Soc.* **2017**, *139*, 8329.
(82) Li, X. G.; Bi, W. T.; Chen, M. L.; Sun, Y. X.; Ju, H. X.; Yan, W. S.; Zhu, J. F.; Wu, X. J.; Chu, W. S.; Wu, C. Z.; Xie, Y. *J. Am. Chem. Soc.* **2017**, *139*, 14889.
(83) Li, Y. H.; Xing, J.; Chen, Z. J.; Li, Z.; Tian, F.; Zheng, L. R.; Wang, H. F.; Hu, P.; Zhao, H. J.; Yang, H. G. *Nat. Commun.* **2013**, *4*, 2500.
(84) Tauster, S. J.; Fung, S. C.; Garten, R. L. *J. Am. Chem. Soc.* **1978**, *100*, 170.
(85) Li, Q. Y.; Wang, K.; Zhang, S. L.; Zhang, M.; Yang, H. J.; Jin, Z. S. *J. Mol. Catal. A: Chem.* **2006**, *258*, 83.
(86) Park, J. Y.; Baker, L. R.; Somorjai, G. A. *Chem. Rev.* **2015**, *115*, 2781.

DOI: 10.1021/jacs.8b03067
J. Am. Chem. Soc. 2018, 140, 7869−7877

(87) Chen, P. R.; Khetan, A.; Yang, F. K.; Migunov, V.; Weide, P.; Sturmer, S. P.; Guo, P. H.; Kahler, K.; Xia, W.; Mayer, J.; Pitsch, H.; Simon, U.; Muhler, M. *ACS Catal.* **2017**, *7*, 1197.
(88) Silvi, B.; Savin, A. *Nature* **1994**, *371*, 683.
(89) Vidal, A. B.; Feria, L.; Evans, J.; Takahashi, Y.; Liu, P.; Nakamura, K.; Illas, F.; Rodriguez, J. A. *J. Phys. Chem. Lett.* **2012**, *3*, 2275.

DOI: 10.1021/jacs.8b03067
J. Am. Chem. Soc. 2018, 140, 7869−7877